Materials Science & Engineering A 854 (2022) 143823

Contents lists available at ScienceDirect

Materials Science & Engineering A

journal homepage: www.elsevier.com/locate/msea

Particle-reinforced Cu matrix composites fabricated by sintering core–shell-type amorphous/crystalline composite powders

Jiahua Zhu [a,b], Yuanfei Cai [c], Yan Zhang [d], Xiaodi Liu [a], Jinseng Tian [a], Jiang Ma [a,e,*], Jun Shen [a,e]

[a] Shenzhen Key Laboratory of High Performance Nontraditional Manufacturing, College of Mechatronics and Control Engineering, Shenzhen University, Shenzhen, 518060, China
[b] Key Laboratory of Optoelectronic Devices and Systems, College of Physics and Optoelectronic Engineering, Shenzhen University, Shenzhen, 518060, China
[c] School of Materials Science and Engineering, Tongji University, Shanghai, 201804, China
[d] Ningbo Institute of Materials Technology and Engineering, Chinese Academy of Science, Ningbo, 315201, China
[e] Guangdong Key Laboratory of Electromagnetic Control and Intelligent Robots, Shenzhen University, Shenzhen, 518060, China

ARTICLE INFO

Keywords:
Metal matrix composites
Spark plasma sintering
Microstructure
Mechanical property

ABSTRACT

The FeSiB-rich particle-reinforced Cu metal matrix composites (MMCs) were fabricated by sintering core–shell-type composite powders using spark plasma sintering (SPS) technique. Results revealed that the strength (σ_{yc} = 548 MPa and σ_{fc} = 957 MPa) of composites is significantly enhanced without sacrificing ductility (ε = 29%). The increase in strength is mainly attributed to the homogenously distributed FeSiB-rich reinforcements and high interfacial strength between the Cu-rich matrix and reinforcements.

1. Introduction

Particulate-reinforced metal matrix composites (MMCs), such as Cu-, Al-, and Ti-based MMCs, have attracted considerable research interest due to their high stiffness and diverse industrial application prospects [1–8]. Preparation processes of MMC materials primarily include *ex-situ* introduction of reinforcements and liquidus *in-situ* reaction [1,2]. Among these MMCs, typical reinforcements are ceramics in different morphological forms [8–10]. However, the poor interfacial wettability between ceramic particles and the matrix usually leads to agglomeration of ceramic particles, reduction of density of the composite, and ultimate deterioration of the strength of the composite [1,2,10]. In addition, ceramic reinforcements are susceptible to fragmentation during the cooling process due to the large difference in the coefficient of thermal expansion between ceramics and the metal matrix [9–11]. Amorphous alloys (or metallic glasses) exhibit high strength and superplasticity in the supercooled liquid region, which have been suggested as attractive reinforcing agents for MMCs [3–7,12]. Meanwhile, amorphous alloys can increase the strength of MMCs effectively and retain desirable ductility before fracture [5]. Xie et al. [3,4,12] recently carried out numerous studies on amorphous alloy-reinforced Cu MMCs. The researchers carefully investigated the effects of particle size, ball milling time, sintering temperature, and particle volume fraction on the mechanical properties of composites, and obtained Cu-based MMCs with high strength. However, the low crystallization temperature of amorphous alloys and the brittle intermetallic formation after crystallization severely limit their potential as reinforcements.

The following aspects of the amorphous alloy-reinforced MMCs prepared via the *ex-situ* method should be investigated to overcome the abovementioned problems: 1) preparation of composite powders with special structures (e.g., core–shell-type and sandwich-type structures) to ensure the diffuse distribution of the reinforcements, 2) obtain a strong bonding interface between the matrix and reinforcements, and 3) selection of reinforcement with a combination of high strength and partial plastic deformability. Recently, amorphous/crystalline composite powders with a core–shell-type structure induced by liquid–liquid phase separation (LLPS) have been successfully designed and fabricated in Co (Fe)–Si–B–Cu quaternary alloy system [13,14]. In this work, we intend to investigate the Cu–Fe–Si–B system, which was selected because the Cu–Fe binary system contains a metastable LLPS [15,16]. On the one hand, the FeSiB ternary system is a commercially used amorphous alloy with high glass-forming ability and outstanding magnetic properties,

* Corresponding author. Shenzhen Key Laboratory of High Performance Nontraditional Manufacturing, College of Mechatronics and Control Engineering, Shenzhen University, Shenzhen, 518060, China.
E-mail address: majiang@szu.edu.cn (J. Ma).

https://doi.org/10.1016/j.msea.2022.143823
Received 12 June 2022; Received in revised form 14 August 2022; Accepted 18 August 2022
Available online 26 August 2022

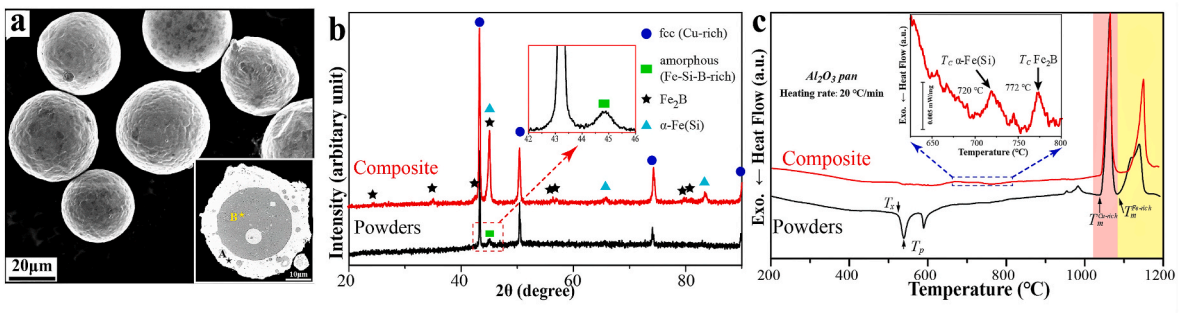

Fig. 1. (a) SEM images of the CuFeSiB composite powders and the inset is the cross-section image; (b) and (c) are the XRD patterns and DSC curves of the CuFeSiB powders and sintered bulk composite.

especially for $Fe_{80}Si_9B_{11}$ (at.%) alloy [17]. On the other hand, Cu-Fi-Si-B composite is a potential electromagnetic interference (EMI) material due to its good electrical and soft magnetic properties [18,19]. Additionally, selecting a suitable powder metallurgical method is also necessary to obtain a densified sintered sample. Spark plasma sintering (SPS) is a rapid consolidation process with a very low sintering temperature and short time [20,21]. During SPS, the high-energy pulsed current (DC) can rapidly activate the powder surface and ultimately obtain high densification. In the present work, FeSiB-rich particle-reinforced Cu MMCs were prepared through gas-atomization and SPS. The microstructures and mechanical properties of the powder and composite were investigated. Interfacial strength, strengthening mechanism, and fracture pattern of the composite were also analyzed.

2. Experimental procedure

$Cu_{55}(Fe_{0.8}Si_{0.09}B_{0.11})_{45}$ (at.%) composite powders (with diameters of about 35 μm) were prepared using a high-pressure argon gas-atomization method. The composite powders were pre-compacted in a graphite die (with an inner diameter of 12 mm) and then sintered with an SPS apparatus (SPS-3.20 MK-II, Wuhan University). The sintering temperature, loading pressure and holding time are 800 °C, 40 MPa and 10 min, respectively. All the preparation process of the composite powders and bulk material are shown in Supplementary Fig. 1. The phase identification, evolution, composition, and microstructure of the sample were characterized via X-ray diffraction (XRD, Rigaku MiniFlex 600), differential scanning calorimetry (DSC, NETZSCH DSC-404F3), scanning electron microscopy (SEM, FEI Quanta 450FEG), and transmission electron microscopy (TEM, JEOL F200) with energy dispersive X-ray spectrometry (EDS, Oxford X-Max). The electron backscatter diffraction (EBSD) characterization was used to determine the grain sizes of the matrix phase. For TEM specimen was thinned mechanically and then argon-ion milled to electron transparency. Rectangular specimens (3 mm × 3 mm × 6 mm) were used to measure compressive mechanical properties with an Instron testing machine at a strain rate of 5×10^{-3} s^{-1}. The hardness and elastic modulus of the composite were measured using nanoindentation tests (nanoindenter, Hysitron TI950), which were carried out using a diamond Berkovich tip. Indentations were performed in the load-control mode with a maximum load of 8 mN at a constant loading–unloading rate of 2 mN/s. Vickers hardness was performed with a load of 0.2 kg for 10 s.

3. Results and discussion

Fig. 1 shows the morphology, microstructure, crystalline structure and characteristic temperatures of the fabricated powder and composite. The powder exhibits a spherical morphology (Fig. 1a) and an inhomogeneous size distribution from 10 μm to 55 μm (Supplementary Fig. 2a). The surface of powders is clean and smooth, and abundant dendritic grains can also be observed. The cross-section image (inset in Fig. 1a) demonstrated that there exists a typical core–shell-type composite microstructure with different phases indicated by the contrast. The extremely smooth interface between the spherical core and the shell is a signature characteristic of the LLPS phenomenon. The EDS results of Points A and B (Supplementary Figs. 2b and 2c) reveals that the bright and dark regions are Cu-rich ($Cu_{89.3}Fe_{7.6}Si_{3.1}$, at.%) and FeSiB-rich ($Cu_{5.5}Fe_{85.2}Si_{9.3}$, at.%) phases, respectively.

Fig. 1b shows the XRD patterns of CuFeSiB composite powders and sintered bulk composite. A series of sharp diffraction peaks corresponding to the *fcc* Cu-rich crystalline phase together with a broad halo peak at about 2θ from 44° to 46° can be clearly seen in the powder's XRD pattern. The broad peak (inset in Fig. 1b) is similar to that of the reported $Fe_{80}Si_9B_{11}$ (at.%) amorphous ribbon [17], thereby indicating that the FeSiB-rich amorphous-phase forms in composite powders. By contrast, the curve of the composite contains not only high peaks of the *fcc* Cu-rich phase but also low peaks of α-Fe(Si) and Fe_2B phases. This

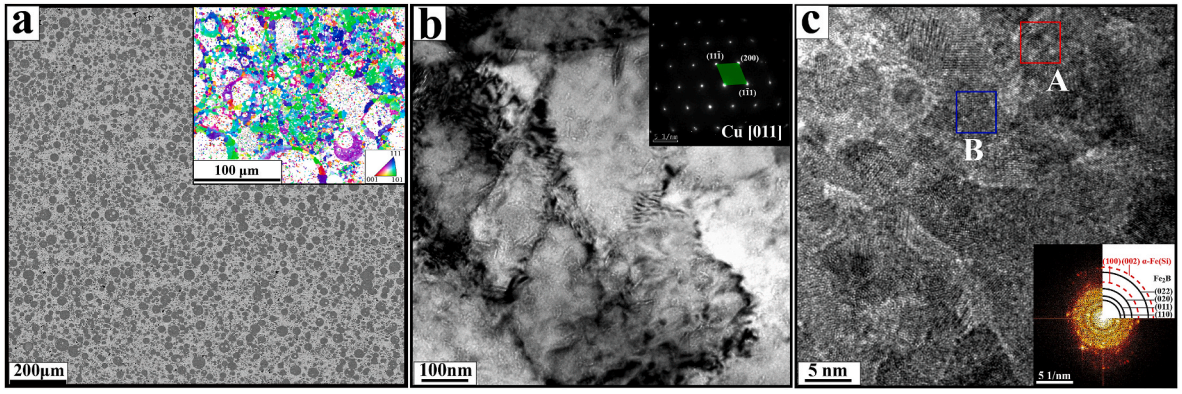

Fig. 2. (a) SEM and EBSD (the inset) images of the sintered composite and Cu-rich phase, respectively; (b) and (c) are the TEM images of the matrix and reinforcements, respectively.

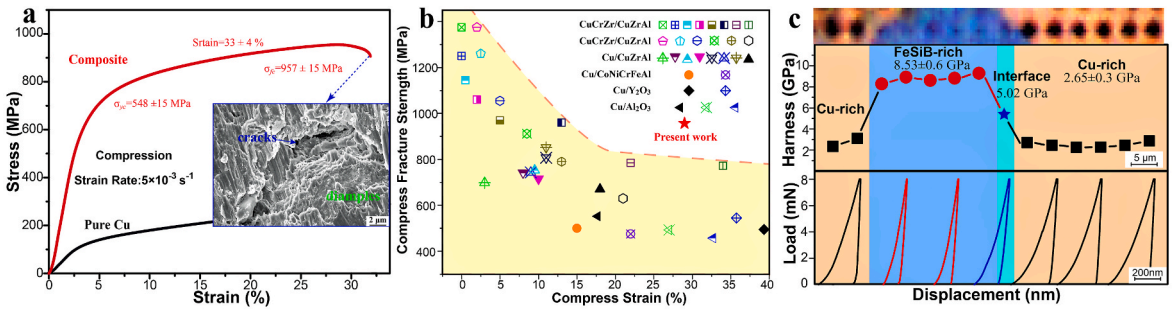

Fig. 3. (a) Compressive strain-stress curves and the fracture surface micrograph (in the inset) of the composites; (b) Scatter plot of the compress strain and fracture stress of particle-reinforced Cu MMCs fabricated by powder metallurgy technology [3,4,12,24–26,32]; (c) Optical microscopy, microhardness and load-displacement curves of the matrix, interface and FeSiB-rich reinforcement.

result confirmed that the FeSiB-rich amorphous phase in powders is completely crystallized during the sintering process. DSC measurement was carried out to identify the formation of amorphous phase and the melting behavior of the composite and powders further, as shown in Fig. 1c. Two sharp exothermic peaks corresponding to amorphous crystallization are observed in the powders. The onset crystallization T_x, and first peak T_p temperatures are about 525 °C and 540 °C, respectively. With the temperature increasing, two weak endothermic transitions (inset in Fig. 1c) occurring at 720 °C and 772 °C correspond to the Curie temperatures (T_C) of Fe_2B and α-Fe(Si) phases, respectively [22,23]. At the high-temperature range, both powders and composite present two endothermic peaks with the onset temperatures of about 1043 °C and 1090 °C, which correspond to the melting of the Cu-rich matrix and the FeSiB-rich phase, respectively.

Fig. 2a displays the microstructure of the bulk composite obtained via SPS. It can be seen that the spherical FeSiB-rich particles were evenly dispersed in the Cu-rich matrix. Meanwhile, there are still a number of hole defects in the sample, which were caused by the low sintering temperature and short sintering time. The EBSD map (inset in Fig. 2a) depicts the microstructure of fcc Cu-rich phase, which exhibited heterogeneous size distribution. The grain sizes of the Cu-rich phase in the matrix and the reinforcement are 1.5 and 3.7 μm, respectively. The element distribution was confirmed through EDS measurements (Supplementary Fig. 3). The interface between the FeSiB-rich phase and the Cu-rich matrix is free of pores and products of interfacial reactions. The microstructure of the bulk composite was further investigated using high resolution TEM and selective area electron diffraction (SAED), as shown in Fig. 2b and 2c. The SEAD pattern inset in Fig. 2b obtained from the Cu-rich matrix conforms to the *fcc* Cu structure, thereby indicating that the crystal structure of the Cu-rich matrix remains unchanged. Fig. 2c shows the HRTEM and corresponding Fast Fourier Transform (FFT) image of the FeSiB-rich phase. Results of the FFT pattern demonstrate that the reinforcement is composed of the α-Fe (Si) and Fe_2B phases. As shown in Supplementary Figs. 4a and 4b, FFT and IFFT images of "A" and "B" regions in Fig. 2c displayed that the crystal structures are α-Fe (Si) and Fe_2B phases, respectively. Furthermore, according to EDS results (Supplementary Fig. 4c), except for the Cu-rich particles, two phases with distinctly different compositions were observed, one of which was enriched in Fe and Si but lacking in Cu and B, while the other was rich in Fe and B but poor in Cu and Si. Herein, the results of XRD, EDS, SASD, FFT, and IFFT generally indicated that sintered composites are composed of the *fcc* Cu matrix and α-Fe (Si) and Fe_2B reinforcements.

Fig. 3a presents the typical uniaxial compression strain–stress curves at ambient temperature for the as-sintered composite together with pure Cu. Mechanical properties of sintered composites are significantly improved compared with pure Cu. The yield strength σ_{yc} (548 ± 15 MPa) and fracture strength σ_{fc} (957 ± 15 MPa) values of the as-sintered composite are higher than those of pure Cu. Additionally, the composite still retains a high plastic strain of about 29%. The inset in Fig. 3a and Supplementary Fig. 5 show the compression fracture micrographs of the composite. These images revealed that several cracks are observed in the matrix after compression. The Cu-rich matrix undergoes large plastic deformation and exhibits ductile fractures with shear zones and dimples. This rupture model is created by the formation and coalescence of microvoids throughout the entire sample. Fig. 3b shows the compression performance comparison of particle-reinforced Cu-based MMCs fabricated by powder metallurgy. Compared with the previously reported Cu-based MMCs, the studied alloy in the present work has the best combination of compressive fracture strength and strain.

For the particle-reinforced MMCs, two classical models (i.e. Voigt and Reuss models) are widely used to analyze the strengthening mechanism. The Voigt model based on the equal strain assumption represents the upper bound of yield strength [27,28]:

$$\sigma_{yc} = f_m\sigma_{ym} + f_p\sigma_{yp} \quad (1)$$

where σ_y is the yield strength; f is the volume fraction; and the subscripts c, m, and p refer to the composite, Cu-rich matrix, and FeSiB-rich particles, respectively. The Reuss model based on the equal stress assumption represents a low bound of yield strength [28,29]:

$$\sigma_{yc} = \left(f_m/\sigma_{ym} + f_p/\sigma_{yp}\right)^{-1} \quad (2)$$

Due to the precipitation and solid solution of Cu element, it is difficult to obtain the yield strength of FeSiB-rich particles. Therefore, σ_{yp} is predicted using an empirical relationship in this study, where the strength is approximately equal to three times of the Vickers hardness [30,31]. Herein, the yield strength of the Cu matrix and FeSiB-rich particles ($Hv_{0.2} \approx 600$) is 120 MPa and 1800 MPa, respectively. By analyzing the SEM image in Fig. 2a, where the volume fractions of the reinforcement and matrix are 40% and 60%, respectively. The yield strength of the present Cu-based MMCs calculated via the Reuss and Voigt models is 792 MPa and 192 MPa, respectively. The experimental value is usually consistent with the results of the Voigt model. While in present study, the σ_{yc} (548 MPa) is closer to Reuss model, thereby indicating that FeSiB-rich particles show significant strengthening efficiency. The strengthening capability of composites (R), that is, the strengthening effect of a given volume percentage of reinforcements on the matrix, can be defined as $(\sigma_{yc} - \sigma_{ym})/f_p\sigma_{ym}$ [32]. The R value of the present work is calculated as 5.9, which is nearly two times higher than that of SiC ($R = 2.5$) and alumina ($R = 2.3$) particle-reinforced Cu-based MMCs [33,34].

Moreover, interfacial bonding was investigated using the nanoindentation test and fracture surface analyses to verify the strengthening efficiency. Fig. 3c shows the nanoindentation results of the composite, including optical image, hardness, and load–displacement curves. The average hardness of Fe-rich particles, interface, and Cu-rich matrix are 8.53 ± 0.6, 5.02, and 2.65 ± 0.3 GPa, respectively. The load–displacement curves showed that the penetration depth at the interface is significantly smaller than that of the Cu-rich matrix and greater than that of FeSiB-rich reinforcement. In addition, nanoindentation

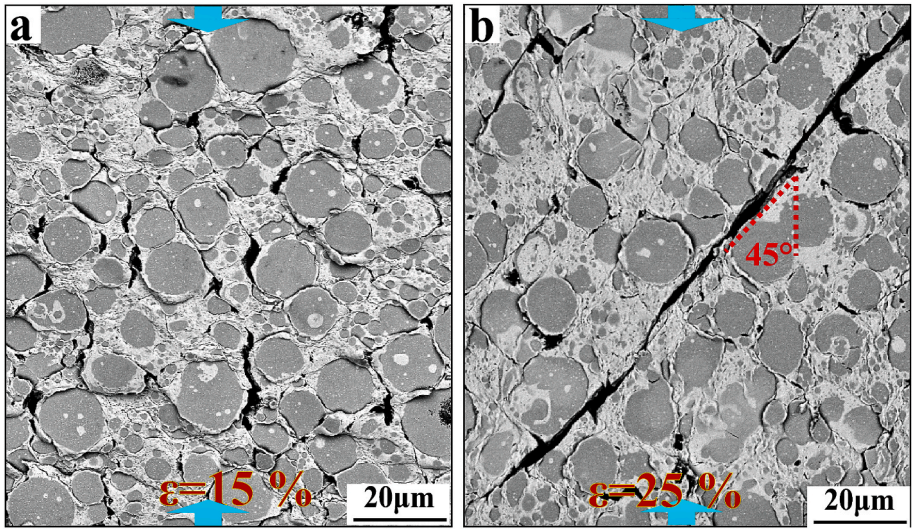

Fig. 4. (a) and (b) are the SEM images of the lateral surface of the composite at strains of 15% and 25%, respectively.

experiments on the composites under a large load of 100 mN were also conducted and the results are shown in Supplementary Fig. 6. It can be seen that the experimental results are in full agreement with the small load of 8 mN. Meanwhile, no cracks appeared around the indentation at the interface, which further demonstrates the good interfacial bonding of the composite.

The morphology of lateral surfaces after compression was further examined via SEM to investigate deformation processes, crack formation and propagation of the composite, as shown in Fig. 4a and 4b. Some discontinuous cracks are preferentially formed around reinforcement particles with large diameters in the case of composites with a compressive strain of 15% (Fig. 4a). As the strain increases to 25% (Fig. 4b), small cracks expand and ultimately develop into large cracks, which are formed along the planes of the maximum shear stress at an approximately incline of 45° to the loading axis. Notably, minimal fragmentation of the FeSiB-rich reinforcement throughout the deformation process verified that the FeSiB-rich particle has both high strength and plasticity. Generally, the plasticity of Fe-based amorphous alloys after crystallization is extremely limited [35], whereas the FeSiB-rich reinforcements in this study exhibit relatively higher plasticity. This is primarily due to the high volume fraction of the solid solution phase of α-Fe (Si) and the multi-scale plastic Cu-rich phase in FeSiB-rich particles. As a result, cracks can only generate in the weak Cu-rich matrix during deformation, which is another important reason for the high strength and plasticity of the composite.

4. Conclusions

In summary, high-strength Cu MMCs with FeSiB-rich reinforcements were successfully synthesized through the SPS process using composite powders with the FeSiB-rich amorphous core and Cu-rich crystalline shell. FeSiB-rich particles in the sintered composite were composed of α-Fe (Si) and Fe_2B phases and uniformly distributed in the Cu-rich matrix. The composite exhibits increased compressive strength and strengthening efficiency and also maintains satisfactory plasticity. The mechanism of strength enhancement of composites is the homogenously distributed FeSiB-rich particles and the high strength of the matrix–reinforcement interface.

Originality statement

I write on behalf of myself and all co-authors to confirm that the results reported in the manuscript are original and neither the entire work, nor any of its parts have been previously published. The authors confirm that the article has not been submitted to peer review, nor has been accepted for publishing in another journal. The author(s) confirms that the research in their work is original, and that all the data given in the article are real and authentic. If necessary, the article can be recalled, and errors corrected.

CRediT authorship contribution statement

Jiahua Zhu: Conceptualization, Formal analysis, Methodology, Writing – original draft. **Yuanfei Cai:** Formal analysis. **Yan Zhang:** Methodology, Writing – review & editing. **Xiaodi Liu:** Methodology, Writing – review & editing. **Jinseng Tian:** Investigation, Writing – review & editing. **Jiang Ma:** Supervision, Writing – review & editing. **Jun Shen:** Supervision, Writing – review & editing.

Declaration of competing interest

The authors declare that they have no known competing financial interests or personal relationships that could have appeared to influence the work reported in this paper.

Data availability

Data will be made available on request.

Acknowledgements

This work was financial supported by the National Natural Science Foundation of China (No. 52071217), the National Key Research and Development Program of China (No. 2018YFA0703605), and the Guangdong Key Laboratory of Electromagnetic Control and Intelligent Robots. The authors are grateful for the technical assistance from the Instrumental Analysis Center of Shenzhen University.

Appendix A. Supplementary data

Supplementary data to this article can be found online at https://doi.org/10.1016/j.msea.2022.143823.

References

[1] T.W. Clyne, P.J. Withers, An Introduction to Metal Matrix Composites, Cambridge University Press, 1993.
[2] N. Chawla, K.K. Chawla, Metal Matrix Composites, Springer, 2013.

[3] J. Chen, B.H. Li, W.Z. Bao, Z.Y. Cai, G.Q. Xie, Achieving high strength and high conductivity of bulk metallic glass composites by controlled milling process, J. Alloys Compd. 902 (2022), 163849.
[4] W.Z. Bao, J. Chen, X.X. Yang, T. Xiang, Z.Y. Cai, G.Q. Xie, Improved strength and conductivity of metallic-glass-reinforced nanocrystalline CuCrZr alloy, Mater. Des. 214 (2022), 110420.
[5] Z. Wang, K. Georgarakis, K.S. Nakayama, Y. Li, A.A. Tsarkov, G. Xie, D. Dudina, D. V. Louzguine-Luzgin, A.R. Yavari, Microstructure and mechanical behavior of metallic glass fiber-reinforced Al alloy matrix composites, Sci. Rep. 6 (2016), 24384.
[6] H.D. Guan, C.J. Li, P. Gao, K.G. Prashanth, J. Tan, J. Eckert, J.M. Tao, J.H. Yi, Aluminum matrix composites reinforced with metallic glass particles with core-shell structure, Mater. Sci. Eng. 771 (2020), 138630.
[7] L.P. Huang, W. L Tan, S. Li, Y. M Li, Effect of loading pressure on mechanical properties and interface characteristics of 7056 Al alloy particle reinforced Zr-Al-Ni-Cu bulk metallic glass matrix composite prepared by spark plasma sintering, J. Alloys Compd. 816 (2020), 152605.
[8] Q. Wang, Z.H. Zhang, T.J. Su, X.W. Cheng, X.Y. Li, S.Z. Zhang, J.Y. He, A TiB whisker-reinforced titanium matrix composite with controllable orientation: a novel method and superior strengthening effect, Mater. Sci. Eng. 830 (2022), 142309.
[9] J. Liu, S. Yang, W. Xia, X. Jiang, C. Gui, Microstructure and wear resistance performance of Cu-Ni-Mn alloy based hardfacing coatings reinforced by WC particles, J. Alloys Compd. 654 (2016) 63–70.
[10] L.M. Kang, Y.J. Cai, X.C. Luo, Z.J. Li, X.B. Liu, Z. Wang, Y.Y. Li, C. Yang, Bimorphic microstructure in Ti-6Al-4V alloy manipulated by spark plasma sintering and in-situ press forging, Scripta Mater. 193 (2021) 43–48.
[11] M.X. Guo, K. Shen, M.P. Wang, Relationship between microstructure, properties and reaction conditions for Cu–TiB2 alloys prepared by in situ reaction, Acta Mater. 57 (2009) 4568–4579.
[12] W.Z. Bao, H. Yan, J. Chen, G.Q. Xie, High strength conductive bulk Cu-based alloy/metallic glass composites fabricated by spark plasma sintering, Mater. Sci. Eng. 825 (2021), 141919.
[13] Y. Yu, Y. Takaku, M. Nagasako, C.P. Wang, X.J. Liu, R. Kainuma, K. Ishida, Liquid-immiscibility-induced formation of micron-scale crystalline/amorphous composite powder, Intermetallics 25 (2012) 95–100.
[14] X. Liu, J. Zhu, Y. Yu, J. Zhang, S. Yang, C. Wang, In situ formation of amorphous-core/crystalline-shell composite powder in liquid immiscible Fe-Si-B-Cu system, Rare Met. Mater. Eng. 49 (2020) 109–115.
[15] C.P. Wang, X.J. Liu, I. Ohnuma, R. Kainuma, K. Ishida, Formation of immiscible alloy powders with egg-type microstructure, Science 297 (2002) 990–993.
[16] C.P. Wang, X.J. Liu, R.P. Shi, C. Shen, Y.Z. Wang, I. Ohnuma, R. Kainuma, K. Ishida, Design and formation mechanism of self-organized core/shell structure composite powder in immiscible liquid system, Appl. Phys. Lett. 91 (2007), 141904.
[17] H. Lee, A.Y. Lee, K.Il Kim, H. Jeong, S.A. Hong, M. Kim, K. Lee, K.T. Kim, Nano-crystallization behavior and magnetic domain evolution in commercial Fe-Si-B metallic glass, J. Alloys Compd. 857 (2021), 157565.
[18] J. Zhang, J. Li, G. Tan, R. Hu, J. Wang, C. Chang, X. Wang, Thin and flexible Fe-Si-B/Ni-Cu-P metallic glass multilayer composites for efficient electromagnetic interference shielding, ACS Appl. Mater. Interfaces 9 (48) (2017) 42192–42199.
[19] Z. Ma, J. Li, J. Zhang, A. He, Y. Dong, G. Tan, M. Ning, Q. Man, X. Liu, Ultrathin, flexible, and high-strength Ni/Cu/metallic glass/Cu/Ni composite with alternate magneto-electric structures for electromagnetic shielding, J. Mater. Sci. Technol. 81 (2021) 43–50.
[20] L. Huang, M. Qian, Z. Liu, V.T. Nguyen, L. Yang, L. Wang, J. Zou, In situ preparation of TiB nanowires for high-performance Ti metal matrix nanocomposites, J. Alloys Compd. 735 (2018) 2640–2645.
[21] C.J. Yan, S. Guo, R.J. Chen, D. Lee, A.R. Yan, Phase constitution and microstructure of Ce–Fe–B strip-casting alloy, Chin. Phys. B 23 (2014), 107501.
[22] D. Wang, L. Ma, L. Li, X.L. Xu, Y.B. Guo, S.Q. Zhao, Characterization of polycrystalline Fe_2B compound with high saturation magnetization, J. Supercond. Nov. Magnetism 31 (2018) 431–435.
[23] Z.Y. Hu, Z.H. Zhang, X.W. Cheng, F.C. Wang, Y.F. Zhang, S.L. Li, A review of multiphysical fields induced phenomena and effects in spark plasma sintering: fundamentals and applications, Mater. Des. 191 (2020) 108662–108716.
[24] J. Chen, P. Niu, T. Wei, L. Hao, Y. Liu, X. Wang, Y. Peng, Fabrication and mechanical properties of AlCoNiCrFe high-entropy alloy particle reinforced Cu matrix composites, J. Alloys Compd. 649 (2015) 630–634.
[25] A. Munoz, B. Savoini, M.A. Monge, Y. Ortega, O.J. Dura, Fabrication and characterization of Cu reinforced with Y-enriched particles following a novel powder metallurgy route, Nucl. Mater. Energy. 29 (2021), 101075.
[26] A. Fathy, F. Shehata, M. Abdelhameed, M. Elmahdy, Compressive and wear resistance of nanometric alumina reinforced copper matrix composites, Mater. Des. 36 (2012) 100–107.
[27] S. Scudino, G. Liu, K.G. Prashanth, B. Bartuscha, K.B. Surreddi, B.S. Murty, J. Eckert, Mechanical properties of Al-based metal matrix composites reinforced with Zr-based glassy particles produced by powder metallurgy, Acta Mater. 57 (2009) 2029–2039.
[28] H.S. Kim, On the rule of mixtures for the hardness of particle reinforced composites, Mater. Sci. Eng. 289 (2000) 30–33.
[29] D.V. Dudina, K. Georgarakis, M. Aljerf, Y. Li, M. Braccini, A.R. Yavari, A. Inoue, Cu-based metallic glass particle additions to significantly improve overall compressive properties of an Al alloy, Compos. Part A. Appl. Sci. Manuf. 41 (2010) 1551–1557.
[30] J.R. Cahoon, W.H. Broughton, A.R. Kutzak, The determination of yield strength from hardness measurements, Metall. Trans. A 2 (1971) 1979–1983.
[31] P. Zhang, S.X. Li, Z.F. Zhang, General relationship between strength and hardness, Mater. Sci. Eng. 529 (2011) 62–73.
[32] S.I. Cha, K.T. Kim, S.N. Arshad, C.B. Mo, S.H. Hong, Extraordinary strengthening effect of carbon nanotubes in metal-matrix nanocomposites processed by molecular-level mixing, Adv. Mater. 17 (2005) 1377–1381.
[33] E. Martinez-Flores, J. Negrete, G.T. Villasenor, Structure and properties of Zn–Al–Cu alloy reinforced with alumina particles, Mater. Des. 24 (2003) 281–286.
[34] Žaklina Gnjidić, Dušan Božić, Mirjana Mitkov, The influence of SiC particles on the compressive properties of metal matrix composites, Mater. Char. 47 (2001) 129–138.
[35] H.X. Li, Z.C. Lu, S.L. Wang, Y. Wu, Z.P. Lu, Fe-based bulk metallic glasses: glass formation, fabrication, properties and applications, Prog. Mater. Sci. 103 (2019) 235–318.